Scilight

Photochemistry and Spectroscopy
https://www.sciltp.com/journals/ps

Article

Excitation Energies in a Polarizable Environment: A Comparison of State-Averaged and Linear-Response CASSCF/AMOEBA Formulations

Tommaso Nottoli, Lorenzo Lapi, Giacomo Londi, Filippo Lipparini and Benedetta Mennucci *

Dipartimento di Chimica e Chimica Industriale, Università di Pisa, Via G. Moruzzi 13, I-56124 Pisa, Italy
* Correspondence: benedetta.mennucci@unipi.it

How To Cite: Nottoli, T.; Lapi, L.; Londi, G.; et al. Excitation Energies in a Polarizable Environment: A Comparison of State-Averaged and Linear-Response CASSCF/AMOEBA Formulations. *Photochemistry and Spectroscopy* **2026**, *2*(1), 10. https://doi.org/10.53941/ps.2026.100010

Received: 10 December 2025
Revised: 9 January 2026
Accepted: 13 January 2026
Published: 5 March 2026

Abstract: Accurate modeling of excitation energies in complex environments is essential for interpreting spectroscopic signatures. A central challenge which is relevant to many systems, is achieving a balanced description of excited states with distinct electronic characters, such as locally excited (LE) and charge transfer (CT) states, while consistently incorporating environmental effects. Here, we compare the linear-response (LR) and state-averaged (SA) formulations of CASSCF when coupled to the polarizable AMOEBA force field. Using the LE and CT excitations of the substrate–cofactor pair in the photoenzyme *Cv*FAP as a test case, we show that LR- and SA-CASSCF offer complementary strengths. LR-CASSCF provides an unbiased mapping of the excitation manifold, whereas SA-CASSCF can refine selected states to obtain a more quantitative description. This combined strategy offers a robust framework for interpreting spectroscopic features of embedded chromophores, especially in systems where CT character and environmental polarization play a decisive role.

Keywords: CASSCF; linear response; state averaged; AMOEBA; polarizable

1. Introduction

The accurate simulation of energies and properties of molecules in electronically excited states remains one of the central challenges in quantum chemistry. This task becomes particularly demanding for large conjugated systems embedded in heterogeneous or strongly interacting environments, where electronic delocalization and environmental effects couple in complex ways. Capturing these features with predictive reliability requires methods that combine electronic-structure accuracy and robustness with computational efficiency, while properly accounting for the influence of solvents, biomolecular matrices, or other complex surroundings.

In many practical scenarios, time-dependent density functional theory (TD-DFT) is the only viable option, thanks to its favorable compromise between accuracy and computational cost. Its efficiency enables the treatment of large molecular systems and, when necessary, the explicit inclusion of selected components of the environment to capture key specific interactions. Furthermore, TD-DFT can be easily integrated with classical descriptions of the environment, such as continuum solvation models or molecular mechanics–based approaches, thus allowing the incorporation of both bulk effects and specific interactions at a computational cost that remains tractable for large and complex systems.

Despite these advantages, TD-DFT suffers from well-known limitations that undermine its reliability in critical cases. A prominent example is its inadequate description of long-range charge-transfer (CT) excitations, which often leads to substantial errors in excitation energies and excited-state character. Although numerous exchange–correlation functionals—particularly long-range corrected and range-separated hybrids—have been developed to alleviate these deficiencies, their performance remains system-dependent and falls short of delivering the robustness required for general predictive applications. This issue becomes especially severe when one aims to describe, with comparable accuracy, excited states of fundamentally different nature, such as locally excited (LE) and

CT states. In principle, wavefunction-based methods could overcome these limitations, but their application to large systems is still hindered by prohibitive computational costs.

The differences between TD-DFT and wavefunction-based approaches in predicting excitation energies and related properties become even more pronounced when these quantum-mechanical descriptions are embedded in a polarizable environment. The influence of such an environment on the excitation process of an embedded molecule is multiple. First, the environment alters the relative energies of the electronic states involved in the transition through the distinct polarization induced by each state. In addition, the environment responds dynamically to the excitation process itself, introducing a contribution associated with a dispersion-like term that originates from its response to fluctuations in the molecular electronic density [1]. In the literature, these two contributions are commonly referred to as the State-Specific (SS) and Linear-Response (LR) terms, respectively [2–5].

Computational studies on various embedded chromophores have shown that only by including both effects—arising from the mutual polarization between the chromophore and its environment—can the full spectral tuning be accurately reproduced [4,6,7]. The SS contribution requires the evaluation of the excited-state electronic density of the quantum subsystem and is therefore naturally compatible with wavefunction-based approaches such as Complete Active Space Self-Consistent Field (CASSCF). In contrast, the LR contribution depends on the transition density associated with the targeted excitation and is inherently accounted for in linear-response formalisms such as TD-DFT.

Recently, some of the present authors have developed a new implementation of the CASSCF method [8–12] that exploits the Cholesky decomposition (CD) of two-electron integrals [13–18] to achieve significant computational savings. This implementation, integrated into the CFOUR suite of programs [19,20], relies on a robust second-order optimization scheme [21–23] for computing the CASSCF wavefunction. It enables the calculation of ground- and excited-state energies, molecular structures, and both static and dynamic response properties [24,25], for which we have developed particularly stable numerical procedures [26,27]. Coupling CASSCF approaches with classical models of the environment is far from trivial, especially when mutual polarization effects between the QM and classical subsystems must be included. Early implementations relied on simplified continuum descriptions of the environment [28], whereas more recent developments have introduced polarizable QM/MM schemes [29–36]. Within this framework, the most widely adopted strategy relies on state-averaged (SA) CASSCF, which provides a balanced description of multiple excited states within a common set of molecular orbitals. During the CASSCF optimization, the environment's polarization is driven to self-consistency with the state-averaged electronic density of the quantum subsystem. However, to recover a physically meaningful, state-specific polarization response for each individual excitation, which is crucial when states differ significantly in charge distribution, an additional corrective step is typically introduced. This correction re-polarizes the environment according to the density of each specific state, thereby improving the accuracy of excitation energies and related properties [30].

This strategy has been recently applied to couple CASSCF with the AMOEBA polarizable force field [37] by using an interface between OPENMMPOL [38], an open-source library which couples QM codes with MM models, and a development version of the CFOUR quantum chemistry software suite. The implementation supports both single-point energy calculations and geometry optimizations. In this work, we extend the CFOUR-OPENMMPOL interface to enable LR-CASSCF calculations, building upon our recent implementation [25,27].

In order to investigate the performance of the LR and SA-CASSCF/AMOEBA formulations, we chose as example a photoenzyme, known as *Chlorella variabilis* fatty acid photodecarboxylase (*Cv*FAP). In a nutshell, *Cv*FAP catalyzes the redox-neutral, light-driven decarboxylation of free fatty acids to yield C1-shortened n-alka(e)nes without requiring external cofactors [39,40]. Its non-covalently bound oxidized flavin adenine dinucleotide (FAD) serves simultaneously as cofactor and chromophore (see Figure 1). Upon absorbing blue or violet light, FAD reaches its singlet locally excited state, becoming a strong oxidant capable of abstracting an electron from the deprotonated fatty acid in the active site. The protein-driven electron transfer is favored by structural rearrangements taking place within the enzyme's active site, which in turn contribute to the stabilization of the CT state's energy at the expense of the LE state on FAD.

First, we provide a brief overview of the CASSCF/AMOEBA implementation in both its state-averaged and newly developed linear-response formulations. We then present the results obtained for the LE and CT states of *Cv*FAP, using TD-DFT/AMOEBA calculations for comparison.

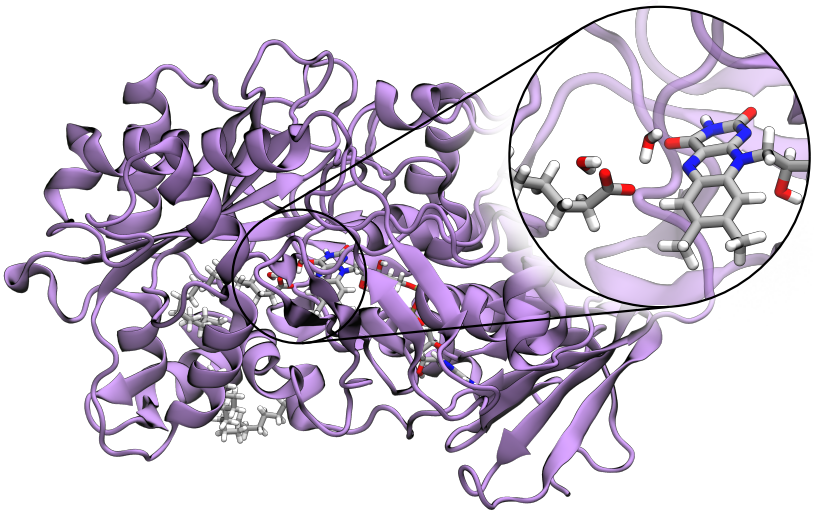

Figure 1. Representation of *Cv*FAP with the active site highlighted in the inset. RSCB PDB entry: 6YRU (https://doi.org/10.2210/pdb6YRU/pdb)

2. Methods

Following the notation and general scheme of Ref. [41], the AMOEBA force field is defined by a fixed multipolar distribution, including charges (q), dipoles (μ^s), and quadrupoles (Q), that are borne by each MM atom and a polarization distribution represented via induced point dipoles (IPDs). We recall that AMOEBA, due to different screening rules used in the polarization step and in energy calculations, introduces two independent sets of induced dipoles that are called 'polarization'(μ^p) and 'direct' (μ^d) [37].

The Lagrangian employed to describe a QM system interacting with the AMOEBA environment is

$$\begin{aligned}\mathcal{L}(\kappa, c, \mu^d, \mu^p) =& \mathcal{E}^{\mathrm{CAS}}(\kappa, c) + \mathcal{E}^{\mathrm{self}}(M) + \mathcal{E}^{\mathrm{ele}}(\kappa, c, M) - \frac{1}{2}\langle \mu^d, \mathbf{E}(\kappa, c) + \mathbf{E}^p(M)\rangle \\ &+ \frac{1}{2}\langle \mu^p, \mathbf{T}\mu^d - \mathbf{E}(\kappa, c) - \mathbf{E}^d(M)\rangle,\end{aligned} \tag{1}$$

where $\mathcal{E}^{\mathrm{CAS}}(\kappa, c)$ is the total CASSCF energy, which depends only on the QM parameters. The underlying wavefunction Ansatz used to obtain this energy is

$$|\Psi\rangle = e^{\hat{\kappa}} \frac{|0\rangle + \hat{P}\,|c\rangle}{1 + \langle c|\,\hat{P}\,|c\rangle} \tag{2}$$

with $\hat{\kappa}$ expressed in terms of antisymmetrized single-excitation operators $\hat{E}^-_{pq}$ and orbital parameters κ_{pq}. Here, $|0\rangle$ is the current expansion point, $|c\rangle$ a CI vector, while $\hat{P} = 1 - |0\rangle\langle 0|$ is the orthogonal projector [42].

The term

$$\mathcal{E}^{\mathrm{self}}(M) = \frac{1}{2}\sum_{k\neq l=1}^{N_{\mathrm{MM}}} s^m_{kl} \sum_{L,L'=0}^{2} M^L_k T^{LL'}_{kl} M^{L'}_l \tag{3}$$

is the self-interaction energy of the multipolar distribution (M^L), with $L = 0, 1, 2$ corresponding to charges, dipoles, and quadrupoles, respectively. The factor s^m_{kl} screens short-range interactions to remove spurious contributions,

$$T^{LL'}_{kl} = \frac{\partial^L}{\partial r^L_k}\frac{\partial^{L'}}{\partial r^{L'}_l}\frac{1}{|r_k - r_l|} \tag{4}$$

is the generalized Coulomb kernel, and N_{MM} denotes the number of MM atoms.

$$\mathcal{E}^{\mathrm{ele}}(\kappa, c, M) = \sum_{k=1}^{N_{\mathrm{MM}}}\sum_{L} M^L_k \left(\sum_{\alpha} T^{L0}_{k\alpha} Z_\alpha - \Theta^L_k\right) \tag{5}$$

is the electrostatic interaction energy between the MM multipoles and the QM density and $\Theta^L_k = \langle 0|\,\hat{t}^L_k\,|0\rangle$ is the QM multipole moment (for $L = 0$ the potential, $L = 1$ the electric field, and $L = 2$ the field gradient), and the

second-quantized operator reads

$$\hat{t}_k^L = \sum_{pq} t_{pq,k}^L \hat{E}_{pq}. \tag{6}$$

The second-to-last term in Equation (1) is the AMOEBA polarization energy, which is written as the scalar product between the induced dipoles (μ^d) and the total electric field acting on the MM sites. The total field is the sum of the QM field, $E_k(\kappa, c)$, and the *polarization* field produced by the other MM multipoles

$$E_k^p(M) = -\left(\sum_l s_{kl}^p \sum_L \mathcal{T}_{kl}^{1L} M_l\right), \tag{7}$$

Here $\mathcal{T}_{kl}^{LL'}$ is a damped interaction kernel used to avoid the so-called polarization catastrophe:

$$\mathcal{T}_{kl}^{LL'} = \frac{\partial^L}{\partial r_k^L} \frac{\partial^{L'}}{\partial r_l^{L'}} \frac{\lambda(|r_k - r_l|)}{|r_k - r_l|}, \tag{8}$$

with $\lambda(r)$ the chosen damping function.

Differentiation with respect to μ^d and μ^p leads, respectively, to the following polarization equations

$$\mathbf{T}\boldsymbol{\mu}^d = \mathbf{E}(\kappa, c) + \mathbf{E}^d(M), \tag{9}$$

$$\mathbf{T}\boldsymbol{\mu}^p = \mathbf{E}(\kappa, c) + \mathbf{E}^p(M) \tag{10}$$

The $kl-$th block of matrix $\mathbf{T}$ is defined as follows

$$T_{kl} = \alpha_k^{-1}\delta_{kl} + (1 - \delta_{kl})\mathcal{T}_{kl}^{11}, \tag{11}$$

where α_k is the polarizability of the k-th MM atom. In our implementation, the AMOEBA polarization equations are solved via an efficient iterative solver [43], and linear scaling in computational cost is achieved by using the Fast Multipole Method [44–46].

The coupled CASSCF/AMOEBA equations can be obtained by imposing the stationarity conditions on the Lagrangian. In particular, the gradient with respect to a generic CASSCF parameter ($\lambda = (\kappa, c)$) reads:

$$\frac{\partial \mathcal{E}^{\text{env}}}{\partial \lambda_i} = -\sum_{k=1}^{N_{\text{MM}}} \sum_L M_k^L \frac{\partial \Theta_k^L}{\partial \lambda_i} - \frac{1}{2}\sum_{k=1}^{N_{\text{Pol}}} \left(\mu_k^d + \mu_k^p\right) \frac{\partial E_k}{\partial \lambda_i} \tag{12}$$

where the first contribution stems from the static multipolar distribution, while the second one is due to the polarization, with $N_{\text{Pol}} \leq N_{\text{MM}}$ as the number of polarizable atoms. By differentiating Equation (1) with respect to κ_{pq}, we get the orbital part of the gradient,

$$g_{pq} = g_{pq}^0 - \sum_{k=1}^{N_{\text{MM}}} \sum_L M_k^L \langle 0| \left[\hat{E}_{pq}^-, \hat{t}_k^L\right] |0\rangle - \frac{1}{2}\sum_{k=1}^{N_{\text{Pol}}} \left(\mu_k^d + \mu_k^p\right) \langle 0| \left[\hat{E}_{pq}^-, \hat{t}_k^1\right] |0\rangle, \tag{13}$$

which can be assembled using a modified inactive Fock matrix

$$F_{pq}^I = F_{pq}^{0,I} - \sum_{k=1}^{N_{\text{MM}}} \sum_L M_k^L t_{pq,k}^L - \frac{1}{2}\sum_{k=1}^{N_{\text{Pol}}} \left(\mu_k^d + \mu_k^p\right) t_{pq,k}^1, \tag{14}$$

which includes the effects of the environment as additional one-electron contributions. We denoted with a 0 superscript the vacuum contribution. The configurational gradient can be obtained analogously

$$g_I = g_I^0 - 2\sum_{k=1}^{N_{\text{MM}}} \sum_L M_k^L \langle \Phi_I| \hat{P}\hat{t}_k^L |0\rangle - \sum_{k=1}^{N_{\text{Pol}}} \left(\mu_k^d + \mu_k^p\right) \langle \Phi_I| \hat{P}\hat{t}_k^1 |0\rangle \tag{15}$$

Our implementation is also compatible with second-order CASSCF optimization algorithms, for which the Hessian must be evaluated. This, in turn, requires computing the second derivatives of the environment contributions with respect to the general CASSCF parameters, which can be written as

$$\frac{\partial^2 \mathcal{E}^{\text{env}}}{\partial\lambda_i\partial\lambda_j} = -\sum_{K=1}^{N_{\text{MM}}}\sum_{L} M_k^L \frac{\partial^2\Theta_k^L}{\partial\lambda_i\partial\lambda_j} - \frac{1}{2}\sum_{k=1}^{N_{\text{Pol}}}\left(\mu_k^d+\mu_k^p\right)_k \frac{\partial^2 E_k}{\partial\lambda_i\partial\lambda_j} - \sum_{k=1}^{N_{\text{Pol}}}\frac{\partial\mu_k^d}{\partial\lambda_j}\frac{\partial E_k}{\partial\lambda_i} \tag{16}$$

The first two terms are the direct analogues of the gradient environment contributions and are automatically handled by using the modified Fock matrix (see Equation (14)), whereas the last term constitutes an additional contribution stemming from the dependence of the induced dipoles on the CASSCF parameters. Moreover, we note that for the last term only a single set of induced dipoles needs to be computed, since only the QM field depends on the CASSCF parameters; consequently, Equations (9) and (10) are identical and a single polarization equation need to be solved. In the implementation, the Hessian is never constructed explicitly; instead, we evaluate its action on a trial vector, either orbital (v_{pq}) or configurational (v_I). We therefore show below the expressions for the Hessian–vector product with an orbital trial vector (σ^o) and with a configurational trial vector (σ^c)

$$\bar{\sigma}_I^c = \sigma_I^c - \sum_{k=1}^{N_{\text{Pol}}}\sum_J \frac{\partial\mu_k^d}{\partial c_J} v_J \frac{\partial E_k^{\text{el}}}{\partial c_I}, \tag{17}$$

$$\bar{\sigma}_{pq}^c = \sigma_{pq}^c - \sum_{k=1}^{N_{\text{Pol}}}\sum_I \frac{\partial\mu_k^d}{\partial c_I} v_I \frac{\partial E_k^{\text{el}}}{\partial \kappa_{pq}}, \tag{18}$$

$$\bar{\sigma}_I^o = \sigma_I^o - \sum_{k=1}^{N_{\text{Pol}}}\sum_{pq} \frac{\partial\mu_k^d}{\partial \kappa_{pq}} v_{pq} \frac{\partial E_k^{\text{el}}}{\partial c_I}, \tag{19}$$

$$\bar{\sigma}_{pq}^o = \sigma_{pq}^o - \sum_{k=1}^{N_{\text{Pol}}}\sum_{rs} \frac{\partial\mu_k^d}{\partial \kappa_{rs}} v_{rs} \frac{\partial E^{\text{el}}}{\partial \kappa_{pq}}. \tag{20}$$

The contraction of the induced dipoles derivatives with either an orbital or a configurational trial vector is obtained by solving the polarization equation using an effective electric field. This field is constructed from the transition density matrix in the configurational case,

$$\sum_J \frac{\partial E_k}{\partial c_J} v_J = 2\sum_J \langle\Phi_J|\,\hat{P}\hat{t}_k^1\,|0\rangle\, v_J, \tag{21}$$

and from the one-index–transformed density matrix in the orbital case,

$$\sum_{rs} \frac{\partial E_k}{\partial \kappa_{rs}} v_{rs} = \sum_{rs} \langle 0|\left[\hat{E}_{rs}^-, \hat{t}_k^1\right]|0\rangle\, v_{rs} \tag{22}$$

Excitation energies can be obtained using either the state-averaged (SA) or the linear-response (LR) approaches. In the SA-CASSCF approach, the environment polarization is converged with respect to the state-averaged density of the QM system [32]. In order to recover a state-specific polarization of the environment for each excitation, a correction is introduced following the approach proposed by Li et al. [30]: at convergence of the state-average calculation, for the two states involved in the excitation, we compute the induced dipoles using the corresponding state density (γ^X) and we recompute the electrostatic and polarization terms of the energy

$$\mathcal{E}_{\text{corr}}^X = \mathcal{E}^{\text{ele-pol}}(\gamma^X, \mu(\gamma^X)) - \mathcal{E}^{\text{ele-pol}}(\gamma^X, \mu(\bar{\gamma})) \tag{23}$$

Finally, we correct the state-averaged excitation energy ($\Delta\mathcal{E}_{\text{SA}}^{0F}$) to get the state-specific corrected one as it follows:

$$\Delta\mathcal{E}_{\text{SS}}^{0F} = \Delta\mathcal{E}_{\text{SA}}^{0F} + \Delta\mathcal{E}_{\text{corr}}^{0F} \tag{24}$$

$$\Delta\mathcal{E}_{\text{corr}}^{0F} = \mathcal{E}_{\text{corr}}^F - \mathcal{E}_{\text{corr}}^0 \tag{25}$$

where 0 and F indicate the initial and the final state involved in the excitation, respectively.

The LR approach requires one to solve a generalized eigenvalue problem; for CASSCF, in the presence of a polarizable environment, it assumes the following form

$$\begin{pmatrix} \overline{A+B} & 0 \\ 0 & A-B \end{pmatrix}\begin{pmatrix} v^+ \\ v^- \end{pmatrix} = \omega \begin{pmatrix} 0 & -\Sigma \\ -\Sigma & 0 \end{pmatrix}\begin{pmatrix} v^+ \\ v^- \end{pmatrix} \tag{26}$$

We note that both $A + B$ and $A - B$ contain contributions from static multipoles and induced dipoles, that is the first two terms of Equation (16), while the third contribution only enters $A + B$, that is

$$(\overline{A+B})_{ij} = (A+B)_{ij} - \sum_{k=1}^{N_{\mathrm{Pol}}} \frac{\partial \mu_k^d}{\partial \lambda_j} \frac{\partial E_k}{\partial \lambda_i}. \tag{27}$$

As discussed before, this additional contribution requires one to solve the polarization equation at each step of the LR problem, using as the right-hand side the effective field of Equations (21) and (22).

3. LR-CASSCF and SA-CASSCF Results for CT and LE States of *Cv*FAP

We investigated the nature of the excited states of the fatty acid–FAD complex in the active site of *Cv*FAP by analyzing three structures of the active site obtained from (TD)DFT/MM optimizations in our previous work [47]: the ground-state geometry (@opt(GS)), the locally excited configuration (@opt(LE)), and the charge-transfer minimum (@opt(CT)). As discussed in the reference work, the GS and LE structures of the active site are essentially similar, with a water molecule forming a hydrogen bond with one of the carboxylate oxygens of the fatty acid. In contrast, the CT state shows a more substantial structural reorganization. In particular, the hydrogen-bond network is altered: the water molecule rotates to form a new hydrogen bond with the nitrogen of FAD, and this rearrangement is accompanied by a twisting of the fatty acid's carboxylate group (see Figures 2 and S1 in the Supplementary Materials).

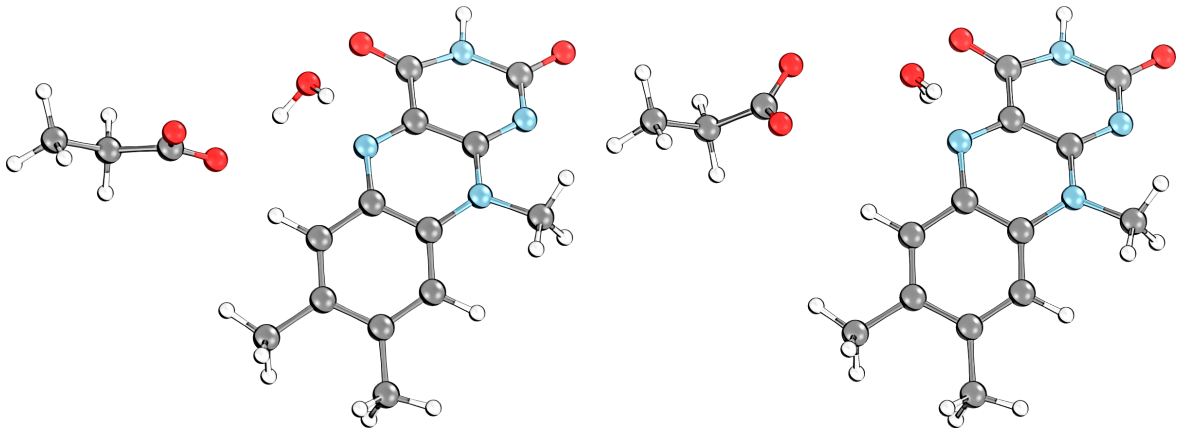

Figure 2. Active site configuration in the @opt(GS) (**left**) and @opt(CT) (**right**) scenarios. Carbon is represented in silver, oxygen in red, nitrogen in blue, and hydrogen in white.

Excitation energies and oscillator strengths were computed employing both Linear-Response CASSCF (LR-CASSCF) and State-Averaged CASSCF (SA-CASSCF). For comparison, TD-DFT calculations were also performed, using the range-separated hybrid ωB97X-D functional, with the standard LR treatment of the polarizable environment as well as by applying a SS correction to the environmental polarization obtained within the so-called corrected linear response (cLR2) scheme originally formulated for continuum models [4]. All QM calculations were carried out using the 6-31G(d) basis set. The basis set choice was validated by performing some calculations using the larger 6-311G(d,p) basis set. The results obtained with the larger basis were in excellent agreement with those obtained with the smaller 6-31G(d) basis, thus justifying our choice.

For each of the three reference geometries, the QM subsystem comprised a truncated fatty acid (the first three carbon atoms including the -COO^- group), the isoalloxazine core of the FAD cofactor, and the bridging water molecule. The remaining portion of the fatty acid and FAD, the protein environment, and the crystallographic water molecules were treated with the polarizable AMOEBA force field. The input file was generated using the `ommp_ip.py` script from the OpenMMPol repository. The script reads the PDB, the Tinker `.xyz` file, the AMOEBA parameters file, and the MDAnalysis selection string used to define the QM and MM regions, and produces a single JSON file containing all the information required to initialize the library.

For the LR-CASSCF calculations, the active space was determined automatically via the unrestricted natural orbitals (UNO) procedure, which resulted in a CAS(8,8) space in the QM/AMOEBA embedding scheme (see Figure S2 in the Supplementary Materials). Notably, this type of selection does not include the low-lying π orbital of the fatty acid's carboxylate group, which does not participate in the multiconfigurational wavefunction. In contrast, the SA-CASSCF calculations were performed starting from converged molecular orbitals of the ground-state

CAS(8,8) calculation. Based on this orbital framework, two active spaces were defined: a CAS(14,8) consistent with that previously employed by Sorigué et al. [40], and a more extensive CAS(14,11) (see Figure S3 in the Supplementary Materials). The CAS(14,8) active space includes three carboxylate π orbitals, four π orbitals on the isoalloxazine core, and a π^* orbital on the same moiety, while the CAS(14,11) further incorporates three additional π^* on the isoalloxazine ring. In the following, we focus our discussion on the CAS(14,11) results. The CAS(14,8) results can be found in the Supplementary Materials and provide a qualitatively similar picture to their CAS(14,11) counterpart. However, a (14,8) active space is very unbalanced, given that only one virtual orbital is present in the definition, and is only appropriate if a subsequent treatment of electronic correlation is applied, as in the work by Sorigué et al. [40]

To investigate the character of the electronic excitations, we examined the natural transition orbitals (NTOs) [48] for each of them. This type of analysis provides a compact representation of the transition density matrices, since it condenses the electronic excitations into a hole-particle orbital pair. The most interesting NTOs arising from the LR-CASSCF calculations are reported in Figure 3, for the first transition of the @opt(GS) and for the first and the seventh transition at @opt(CT) (the analysis of NTOs for @opt(LE), which is very similar to what was obtained at @opt(GS), is reported in Figure S4 of the Supplementary Materials). These NTOs clearly show the LE and CT nature of the corresponding excitations. It is worth noting that LR-CASSCF(8,8), which only includes orbitals localized on the flavine core, is able to describe the CT state.

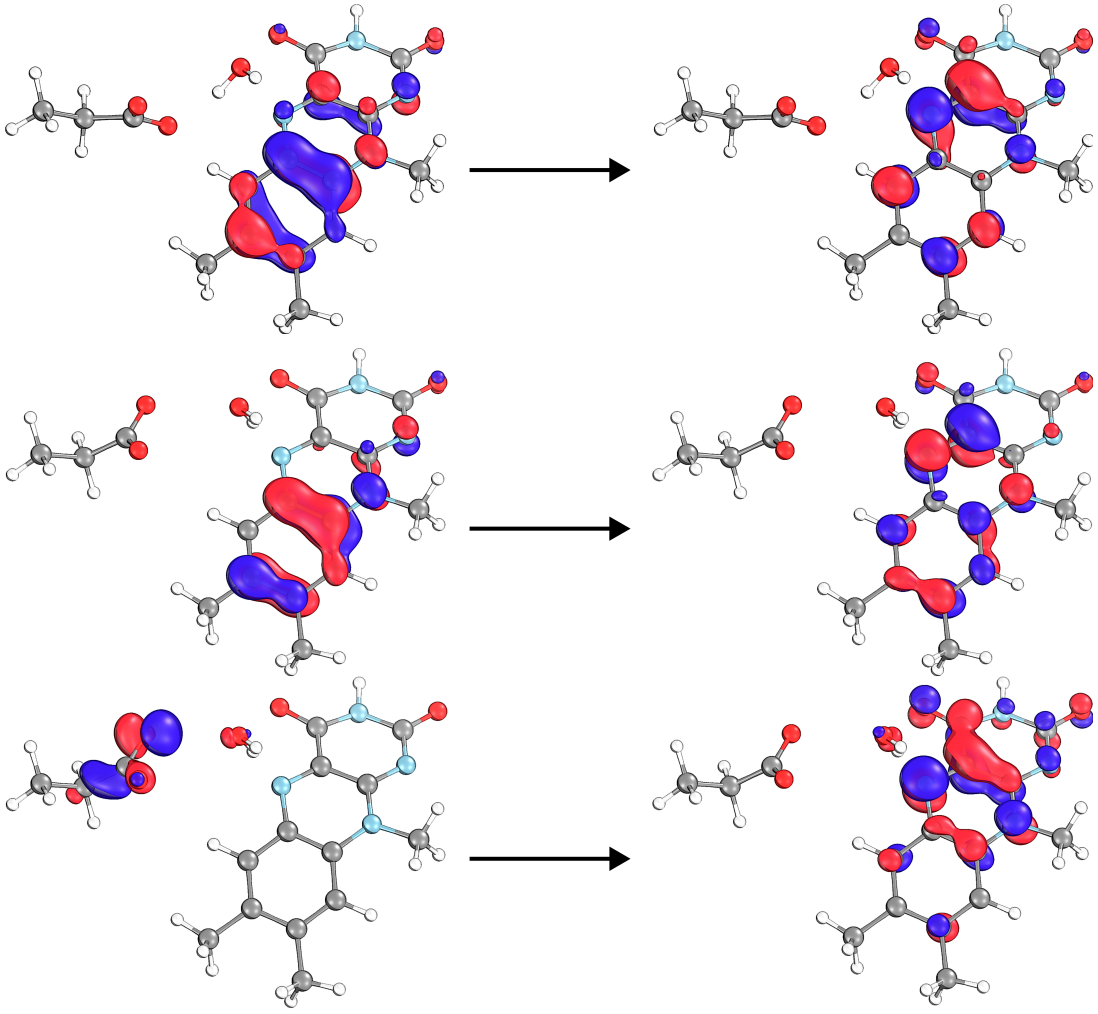

Figure 3. Natural transition orbitals obtained through the LR-CAS(8,8) calculation for the first transition at the @opt(GS) geometry (**top**) and for the first (**central**) and seventh (**bottom**) ones at @opt(CT) geometry.

In Figure 4 we report the NTOs obtained at SA-CAS(14,11) for the first and third transitions at the @opt(CT) geometry. These two transitions clearly represent the CT and LE excitations, respectively.

The excitation energies and the oscillatory strengths for the selected LE and CT states at both LR and SA formulations of CASSCF/AMOEBA are shown in Table 1. In the case of SA-CASSCF, transition energies including the SS correction are also reported. The energies for the full set of states are reported in Table S1 for LR-CAS(8,8), S2 for SA-CAS(14,8), and S3 for SA-CAS(14,11) in the Supplementary Materials.

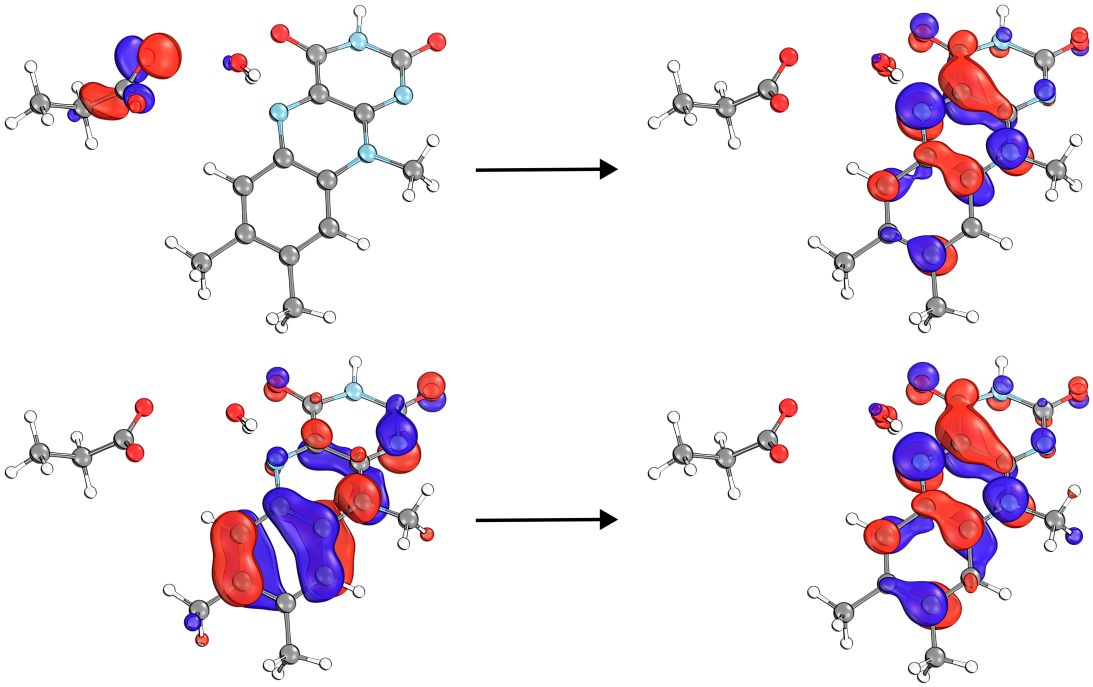

Figure 4. Natural transition orbitals obtained through the SA-CAS(14,11) calculation for the first (**top**) and third (**bottom**) transitions at the @opt(CT) geometry.

Table 1. LR/SA-CASSCF/6-31G(d)/AMOEBA transition energies **E** (eV) and oscillator strengths **f** for the LE and CT states. Calculations were performed at the LR-CASSCF(8,8) level for all geometries. For SA, excitation energies including the state-specific corrections are also shown ($\mathbf{E}_{SA}$/$\mathbf{E}_{SS}$). The state average was over 7 states for the @opt(GS) and @opt(LE) geometries and 6 states for the @opt(CT) geometry.

	@opt(GS)		**@opt(LE)**		**@opt(CT)**	
State	**E**	**f**	**E**	**f**	**E**	**f**
LE(LR)	3.70	0.296	3.03	0.148	3.06	0.316
CT(LR)					5.82	0.004
LE(SA)	3.51/3.49	0.719	2.85/2.84	0.651	2.82/2.80	0.658
CT(SA)	5.99/5.70	0.004	5.41/5.01	0.007	2.59/2.44	0.005

The two CASSCF/AMOEBA formulations provide qualitatively consistent results for the LE state: the corresponding excitation energy decreases significantly when moving from the @opt(GS) to the @opt(LE) geometry, although the magnitude of this red-shift is smaller within the LR formulation, and then it changes only slightly when considering the @opt(CT) structure. However, when we consider the CT state, the two methods start to diverge. For the @opt(GS) and @opt(LE) geometries, both approaches predict the CT state to be strongly destabilized. As a matter of fact, for LR-CASSCF at @opt(GS) and @opt(LE) geometries, the value for the CT transition is not reported as it could not be found in the lowest 14 excitations. At the @opt(CT) structure, the LR formulation describes the CT state at lower energy but still much higher than the LE. On the contrary, the SA treatment yields a substantial stabilization that renders the CT state the lowest in energy. This discrepancy between the two CASSCF formulations is already evident in the gas-phase results (see Table 2), and is due to the uneven treatment that LR-CASSCF provides for the two excitations: while the LE state is well described within the active space and is therefore correlated both at the CAS-CI and particle-hole level, the CT state involves orbitals outside the active space and is thus only affected by the particle-hole correlation.

When environmental effects are taken into account, the LR and SA CASSCF/AMOEBA formulations yield a consistent description for the LE state. Both predict a red-shift relative to the gas phase, with a magnitude increasing progressively from the @opt(GS) to the @opt(LE) and @opt(CT) geometries. This similar behavior is expected, as the SS correction, which is present only in the SA treatment, is small for a locally excited state, whose electronic density differs only modestly from that of the ground state. The situation becomes more complex for the CT transition. In this case, both CASSCF formulations predict a blue-shift with respect to the gas phase. This is consistent with the physical picture: in the isolated system, the CT state is strongly stabilized because the excitation

promotes charge delocalization from the carboxylate group onto the fatty acid–FAD pair. Embedding the system in a polarizable environment largely stabilizes the ground state with the charge localized in the fatty acid and less the CT, thereby shifting the CT excitation to higher energies. Despite the opposite signs of the environmental shifts for LE and CT, the CT transition remains the lowest-energy excitation at the @opt(CT) geometry. This indicates that, although the environment disfavors the CT character relative to the gas phase, the geometric rearrangements accompanying CT formation dominate the energetics and ensure that the CT state is still the energetically preferred excited state at the CT minimum. However, it is interesting to note that the magnitude of the SS correction for CT is larger in the @opt(GS) and @opt(LE) geometries than at the @opt(CT) structure.

Table 2. LR/SA-CASSCF/6-31G(d) gas-phase excitation energies **E** (eV) and oscillator strengths **f** for the LE and CT states. Calculations were performed at the LR-CASSCF(8,8) level for all geometries. For SA, these were computed at the SA-CAS(14,11) level, averaging over 8 states for the @opt(GS) and 6 states for the @opt(LE) and @opt(CT) geometries.

	@opt(GS)		**@opt(LE)**		**@opt(CT)**	
State	**E**	**f**	**E**	**f**	**E**	**f**
LE(LR)	4.07	0.097	3.62	0.148	3.65	0.233
CT(LR)	7.25	0.004	6.50	0.013	4.79	0.000
LE(SA)	3.88	0.603	3.22	0.686	3.73	1.088
CT(SA)	5.56	0.005	4.04	0.001	1.63	0.006

To explain these findings we have compared the electrostatic potential generated on the atoms of the QM subsystem by the AMOEBA induced dipoles in the @opt(GS) and @opt(CT) geometries. The induced dipoles have been calculated using the GS density from the LR-CASSCF/AMOEBA calculation and three different densities from the SA-CASSCF/AMOEBA calculations, SA, GS, and CT, respectively. The results are reported in Figure 5.

As shown in Figure 5, at the @opt(GS) geometry the LR and SA descriptions yield similar electrostatic potentials for their respective ground states. Both reflect the expected behavior of an R-COO$^-$/FAD complex, characterized by large positive electrostatic potentials on the atoms of the anionic carboxylate group of the fatty acid. This situation is reversed in the CT state where the carboxylate group donates an electron to FAD and the electrostatic potential induced by $\mu(\gamma^{CT})$ becomes negative on the fatty acid. The electrostatic potential generated by the AMOEBA dipoles induced by the state-averaged density, $\mu(\bar{\gamma})$, represents an intermediate picture between the GS and CT polarization patterns. When moving from the @opt(GS) to the @opt(CT) geometry, the electrostatic potential due to $\mu(\gamma^{GS})$ undergoes a marked change, becoming strongly negative on FAD. In contrast, the potentials corresponding to $\mu(\gamma^{CT})$ change only slightly relative to those at @opt(GS). As expected, the electrostatic potential arising from $\mu(\bar{\gamma})$ again lies between these two limiting cases.

These results show clearly that the twisting of the charged carboxylate group and the reorganization of the water hydrogen bond in the @opt(CT) geometry have a substantial impact on the ground-state electronic structure of the system, particularly on the electron density localized on FAD. This observation rationalizes why, at this geometry, the state-specific (SS) correction for the CT transition is markedly reduced compared with the other two geometries. The SS contribution is defined as the difference between the CT and GS adjustments relative to the state-averaged picture (see Equation (23)). At the @opt(CT) geometry, these adjustments become similar for the GS and CT states, whereas at the @opt(GS) and @opt(LE) geometries the CT state undergoes a much larger environment-driven redistribution than the GS state.

We now compare the two CASSCF/AMOEBA formulations with TD-DFT/AMOEBA. In the latter case, we report the excitation energies calculated within the standard LR scheme for the response of the polarizable embedding and those in which we have added a state-specific correction calculated on the TD-DFT relaxed densities and the corresponding AMOEBA induced dipoles ($\mathbf{E}_{cLR2}$). The TD-DFT results for the LE and CT excitations are reported in Table 3. The full results are reported in Table S4 in the Supplementary Materials.

As shown in Table 3, the LE state exhibits a qualitatively consistent behavior across TD-DFT and both the LR and SA variants of CASSCF. For this state, the magnitude of the SS correction remains small, in line with expectations. In the case of the CT state, the chosen functional reproduces the SA-CASSCF trends reasonably well at all geometries. However, for TD-DFT the SS correction remains sizable at every structure and shows its largest value at the CT-optimized one.

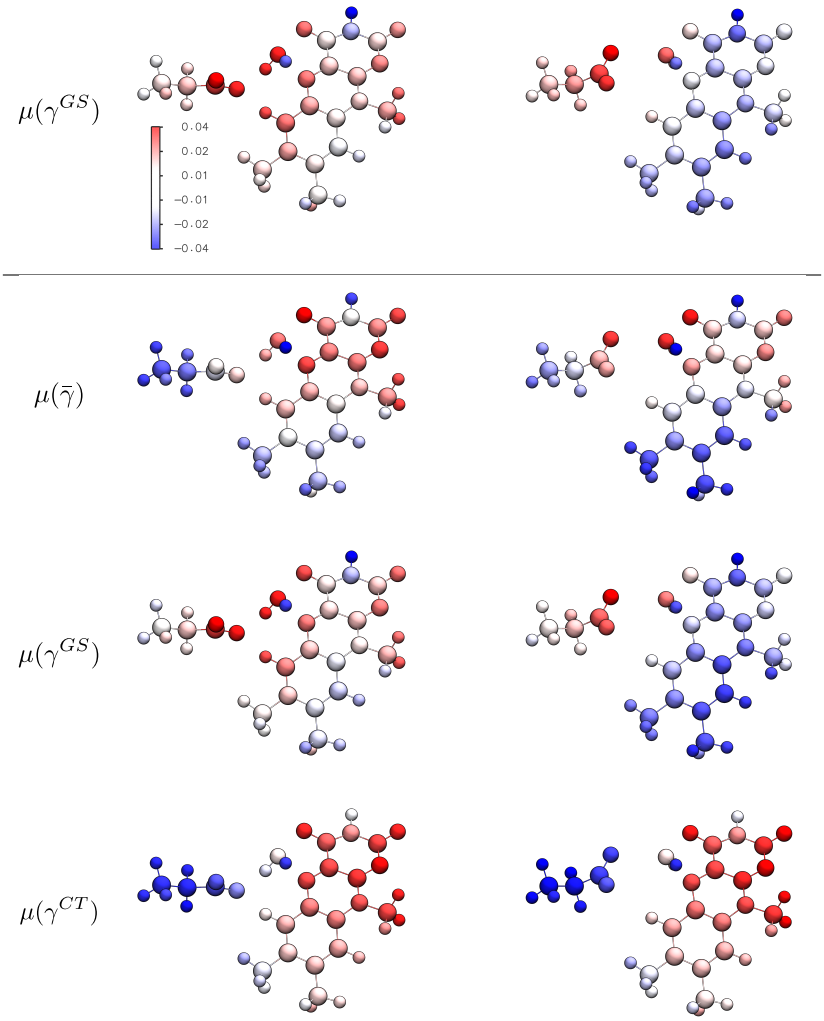

Figure 5. In the (**top panel**), we show the electrostatic potential due to the AMOEBA induced dipoles stemming from the converged ground-state CASSCF density using a CAS(8,8) active space. In the (**bottom panel**), we depict the electrostatic potential due to the induced dipoles stemming from the averaged density at convergence of the SA-CASSCF(14,11) calculation (**top row**), from the GS state density (**central row**) and from the CT density (**bottom row**). The left column shows the results obtained for the @opt(GS) while the right column for the @opt(CT) geometry. The reported values were shifted by their mean to enable a consistent comparison between geometries.

Table 3. TD-DFT/ωB97X-D/6-31G(d)/AMOEBA excitation energies $\mathbf{E}_{LR}$ and their corrected values $\mathbf{E}_{cLR2}$ after including the state-specific corrections $\mathbf{SS}_c$, in eV, and oscillator strengths **f** at the three optimized geometries.

	@opt(GS)			**@opt(LE)**			**@opt(CT)**		
State	$\mathbf{E}_{LR}$	$\mathbf{E}_{cLR2}$	**f**	$\mathbf{E}_{LR}$	$\mathbf{E}_{cLR2}$	**f**	$\mathbf{E}_{LR}$	$\mathbf{E}_{cLR2}$	**f**
LE	3.19	3.17	0.297	2.71	2.69	0.210	2.63	2.61	0.222
CT	4.37	3.66	0.004	3.95	3.23	0.008	1.60	0.67	0.003

As a final analysis, it is interesting to compare all QM/AMOEBA formulations in terms of how the energies of the different states evolve when moving from the Franck–Condon geometry to the structures optimized for the LE and CT states. This analysis shows more clearly how the various approaches capture the relative likelihood of the photoinduced electron-transfer process in the photoenzyme. To enable a direct comparison, all energies were shifted so that each method uses the corresponding ground-state energy at the GS geometry as a common reference. The resulting trends are illustrated in Figure 6. For LR-CASSCF, we report only the GS and LE energies, as the CT state is poorly described by this level of theory.

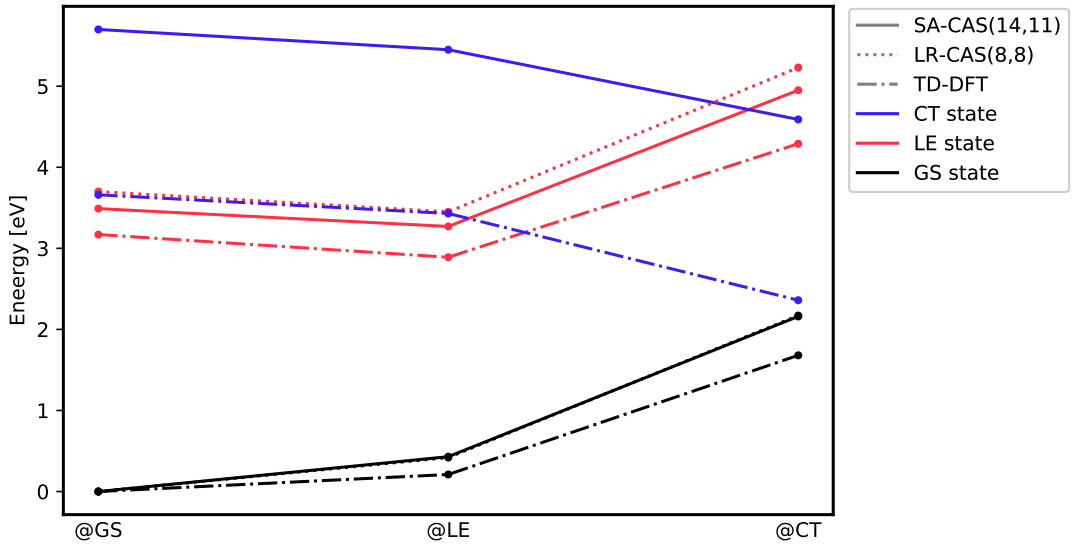

Figure 6. GS (black), LE (red), and CT (blue) energies computed on top of each geometry using as a reference the ground-state energy at the GS geometry. The linestyle denotes the level of theory: solid line for SA-CAS(14,11), dotted line for LR-CAS(8,8), and dash dotted line for TD-DFT. SA-CASSCF and TD-DFT energies include the respective SS corrections.

Overall, the SA-CASSCF and TD-DFT calculations yield qualitatively consistent trends. The LE state exhibits a modest stabilization at the LE geometry which reflects the small geometrical relaxation, followed by a pronounced destabilization at the CT geometry. In contrast, the CT state is progressively stabilized along the same coordinate and becomes the lowest excited state at the CT geometry. Notably, TD-DFT predicts the LE and CT states to lie much closer in energy at both the GS and LE geometries, with a substantial splitting emerging only at the CT geometry. In the SA-CASSCF/AMOEBA results, however, the two states are already well separated at the GS and LE geometries and become significantly closer only at the CT geometry. It is important to note that all geometries considered are true minima only at the (TD-)DFT level, which may lead to a reduced stabilization of each state at its corresponding optimized geometry when evaluated with both LR- and SA-CASSCF.

4. Discussion

In this work, we have presented the extension of the CFOUR-OPENMMPOL interface that includes the newly implemented LR-CASSCF framework, enabling the description of electronic excitations in embedded molecular systems at the CASSCF/AMOEBA level. This allowed us to compare LR- and SA-CASSCF/AMOEBA to study the electronically excited state of the fatty acid-FAD complex in the active site of *Cv*FAP. The main methodological challenge, which is general to many systems, is achieving a consistent and balanced description of excited states with different characters, namely a locally excited (LE) and a charge-transfer (CT) state. This is difficult not only from the electronic structure perspective but also in capturing environmental effects, which are crucial for the correct physics of such systems.

LR-CASSCF offers two key advantages. First, it is as unbiased as CASSCF allows: the active space accounts only for static correlation, not for targeting specific excitations. States that are poorly represented in the active space can still be described thanks to the inclusion of all particle–hole excitations from the ground-state wavefunction. Second, LR-CASSCF provides a better treatment of electron correlation, as both active-space expansion and particle–hole excitations contribute to the excited-state description. However, LR-CASSCF has two main shortcomings. Because states can be described both within the active space and via particle–hole excitations, an unbalanced treatment of states of different nature may arise. Excitations that are well described by the active space benefit from both contributions, whereas those dominated by inactive orbitals rely only on particle–hole terms. This explains why, at the LR level, the CT state of *Cv*FAP is stabilized but remains higher in energy than the LE state. Moreover, LR-CASSCF cannot currently handle state-specific environmental corrections, which are critical for CT states due to large density rearrangements and associated solvation effects.

SA-CASSCF, in contrast, requires that all orbitals involved in the excitation be included in the active space. This makes the method inherently biased, as one is required to already know the nature and main characteristics of an electronic excitation to describe it. Furthermore, the use of averaged orbitals, especially when the electronic states of interest are quite different in nature, offers a reasonable compromise for each state, but is not optimal

for any of them. Finally, the orbitals required to describe an excitation might not be relevant for the treatment of static correlation. This triggers a cascade of numerical issues. The CASSCF optimization may in fact try to rotate an orbital that is required for the description of an excited state out of the active space itself, swapping it for one that is more relevant for strong correlation. Even if one manages to overcome this problem, optimization can exhibit instabilities, root flipping, unwanted local minima, and overall poor convergence. We further remark that larger active spaces are often needed in practice, sharply increasing computational cost. Despite these difficulties, SA-CASSCF allows straightforward state-specific embedding corrections, enabling us to model the inversion in stability between LE and CT states at the CT geometry. It should however be noted that the results are heavily influenced by the choice of the active space, as it can be seen from the comparison between the CAS(14,8) and CAS(14,11) results, and that converging the SA calculations is significantly more difficult for this system.

A final remark concerns the computational cost of LR and SA calculations. LR requires a prior ground-state CASSCF optimization followed by the solution of a generalized eigenvalue problem, whose cost scales with the number of targeted states, making the overall LR effort roughly equivalent to that required for a ground-state second-order CASSCF calculation multiplied by the number of states. For example, a CAS(8,8) LR calculation at the CT geometry required about 4 hours on a dual AMD EPYC 7282 node (32 threads), with 24 min spent on ground-state optimization and the remainder on the LR equations for 10 states. SA calculations are generally cheaper than LR for comparable active spaces. For the same CT geometry, a CAS(14,11) SA calculation for six states required about 15 min. This efficiency arises from the use of a first-order Super-CI solver and from the fact that a single set of orbitals is shared among the various states, which limits the additional cost to the CI step. However, first-order optimization lacks the robustness of second-order methods, making state convergence difficult. Thus, while SA-CASSCF is computationally less demanding, second-order ground-state optimization followed by LR calculations is more black-box, requiring higher computational cost but significantly less human effort.

In conclusion, we believe that LR- and SA-CASSCF are best used in combination. LR-CASSCF can be used to explore the excitation manifold in an unbiased manner, and the results can then be refined using SA-CASSCF to achieve a more quantitative description. Both methods present advantages and shortcomings, but they tend to be complementary. Further developments are nevertheless needed to overcome the difficulties that we have encountered. First, a treatment of electronic correlation is mandatory to achieve quantitative accuracy for both strategies. For LR-CASSCF, the implementation of state-specific corrections, although nontrivial, is also highly desirable. Finally, it is worth underlying that our study shows how sensitive the results can be with respect to the geometry. Therefore, the implementation of analytical gradients for both methods, including the polarizable environment in the picture, looks like a promising direction to further improve their applicability.

Supplementary Materials

The additional data and information can be downloaded at: https://media.sciltp.com/articles/others/260204093353017 5/PS-25120088-Supplementary_Materials.pdf. The supporting information reports tables with excitation energies and oscillator strengths for all the computed states at the LR and SA CASSCF and TD-DFT level of theory, and pictures of the active orbitals used for the CASSCF calculations.

Author Contributions

T.N. and L.L.: Methodology, Software, Investigation, Data Curation, Writing—Original draft, Visualization. G.L.: Methodology, Investigation, Data Curation, Writing—Original draft, Visualization. F.L. and B.M.: Conceptualization, Writing—Original draft, Writing—Review & editing, Supervision, Funding Acquisition. All authors have read and agreed to the published version of the manuscript.

Funding

F.L. acknowledges funding from the Italian Ministry of Research (PRIN 2022) under grant 2022WZ8LME_002. B.M. acknowledges funding from the Italian Ministry of Research (Fondo Italiano per la Scienza, FIS 2) under the grant FIS-2023-00430. G.L. acknowledges the Italian Ministry of University and Research for funding provided by the European Union-NextGenerationEU-PNRR, Missione 4, Componente 2, Linea di investimento 1.2. F.L., T.N. and B.M. further acknowledge financial support from ICSC-Centro Nazionale di Ricerca in High Performance Computing, Big Data, and Quantum Computing, funded by the European Union-NextGenerationEU-PNRR, Missione 4 Componente 2 Investimento 1.4.

Institutional Review Board Statement

Not applicable.

Informed Consent Statement

Not applicable.

Data Availability Statement

Data supporting the findings of this study are available upon request from the corresponding author.

Conflicts of Interest

The authors declare no conflict of interest.

Use of AI and AI-Assisted Technologies

During the preparation of this work, the authors used Microsoft Copilot solely to improve the writing style. The authors reviewed and edited the content as needed, and take full responsibility for the content of the published article.

References

1. Guido, C.A.; Rosa, M.; Cammi, R.; et al. An open quantum system theory for polarizable continuum models. *J. Chem. Phys.* **2020**, *152*, 174114.
2. Corni, S.; Cammi, R.; Mennucci, B.; et al. Electronic excitation energies of molecules in solution within continuum solvation models: Investigating the discrepancy between state-specific and linear-response methods. *J. Chem. Phys.* **2005**, *123*, 134512.
3. Lunkenheimer, B.; Köhn, A. Solvent Effects on Electronically Excited States Using the Conductor-Like Screening Model and the Second-Order Correlated Method ADC(2). *J. Chem. Theory Comput.* **2013**, *9*, 977–994.
4. Guido, C.A.; Jacquemin, D.; Adamo, C.; et al. Electronic Excitations in Solution: The Interplay between State Specific Approaches and a TD-DFT Description. *J. Chem. Theory Comput.* **2015**, *11*, 5782–5790.
5. Schwabe, T. General theory for environmental effects on (vertical) electronic excitation energies. *J. Chem. Phys.* **2016**, *145*, 154105.
6. Guareschi, R.; Valsson, O.; Curutchet, C.; et al. Electrostatic versus Resonance Interactions in Photoreceptor Proteins: The Case of Rhodopsin. *J. Phys. Chem. Lett.* **2016**, *7*, 4547–4553.
7. Nifosì, R.; Mennucci, B.; Filippi, C. The key to the yellow-to-cyan tuning in the green fluorescent protein family is polarisation. *Phys. Chem. Chem. Phys.* **2019**, *21*, 18988–18998.
8. Roos, B.O.; Taylor, P.R.; Siegbahn, P.E.M. A complete active space SCF method (CASSCF) using a density matrix formulated super-CI approach. *Chem. Phys.* **1980**, *48*, 157–173.
9. Roos, B.O. The complete active space self-consistent field method and its applications in electronic structure calculations. *Adv. Chem. Phys.* **1987**, *69*, 399–445.
10. Werner, H.J. Matrix-formulated direct multiconfiguration self-consistent field and multiconfiguration reference configuration-interaction methods. *Adv. Chem. Phys.* **2009**, *69*, 1–62.
11. Olsen, J. The CASSCF method: A perspective and commentary. *Int. J. Quant. Chem.* **2011**, *111*, 3267–3272.
12. Lischka, H.; Nachtigallova, D.; Aquino, A.J.; et al. Multireference approaches for excited states of molecules. *Chem. Rev.* **2018**, *118*, 7293–7361.
13. Beebe, N.H.; Linderberg, J. Simplifications in the generation and transformation of two-electron integrals in molecular calculations. *Int. J. Quant. Chem.* **1977**, *12*, 683–705.
14. Koch, H.; Sánchez de Merás, A.; Pedersen, T.B.; et al. Reduced scaling in electronic structure calculations using Cholesky decompositions. *J. Chem. Phys.* **2003**, *118*, 9481–9484.
15. Pedersen, T.B.; Lehtola, S.; Fdez. Galván, I.; et al. The versatility of the Cholesky decomposition in electronic structure theory. *Wiley Interdiscip. Rev. Comput. Mol. Sci.* **2024**, *14*, e1692.
16. Aquilante, F.; Boman, L.; Boström, J.; et al. Cholesky decomposition techniques in electronic structure theory. In *Linear-Scaling Techniques in Computational Chemistry and Physics: Methods and Applications*; Springer: Dordrecht, The Netherlands, 2011; pp. 301–343.
17. Folkestad, S.D.; Kjønstad, E.F.; Koch, H. An efficient algorithm for Cholesky decomposition of electron repulsion integrals. *J. Chem. Phys.* **2019**, *150*, 194112.
18. Zhang, T.; Liu, X.; Valeev, E.F.; et al. Toward the minimal floating operation count Cholesky decomposition of electron repulsion integrals. *J. Phys. Chem. A* **2021**, *125*, 4258–4265.
19. Stanton, J.F.; Gauss, J.; Cheng, L.; et al. CFOUR, Coupled-Cluster Techniques for Computational Chemistry, a Quantum-Chemical Program Package. Available online: http://www.cfour.de (accessed on 2 February 2026).
20. Matthews, D.A.; Cheng, L.; Harding, M.E.; et al. Coupled-cluster techniques for computational chemistry: The CFOUR program package. *J. Chem. Phys.* **2020**, *152*, 214108.

21. Lipparini, F.; Gauss, J. Cost-effective treatment of scalar relativistic effects for multireference systems: A CASSCF implementation based on the spin-free Dirac–Coulomb Hamiltonian. *J. Chem. Theor. Comput.* **2016**, *12*, 4284–4295.
22. Nottoli, T.; Gauss, J.; Lipparini, F. Second-order CASSCF algorithm with the Cholesky decomposition of the two-electron integrals. *J. Chem. Theory Comput.* **2021**, *17*, 6819–6831.
23. Nottoli, T.; Gauss, J.; Lipparini, F. A black-box, general purpose quadratic self-consistent field code with and without Cholesky decomposition of the two-electron integrals. *Mol. Phys.* **2021**, *119*, e1974590.
24. Nottoli, T.; Burger, S.; Stopkowicz, S.; et al. Computation of NMR shieldings at the CASSCF level using gauge-including atomic orbitals and Cholesky decomposition. *J. Chem. Phys.* **2022**, *157*, 084122.
25. Nottoli, T.; Lapi, L.; Alessandro, R.; et al. An Efficient and Robust Implementation of CASSCF Linear Response Theory. *J. Phys. Chem. A* **2025**, *129*, 8441–8452.
26. Nottoli, T.; Giannì, I.; Levitt, A.; et al. A robust, open-source implementation of the locally optimal block preconditioned conjugate gradient for large eigenvalue problems in quantum chemistry. *Theor. Chem. Acc.* **2023**, *142*, 69.
27. Alessandro, R.; Giannì, I.; Pes, F.; et al. Linear response equations revisited: A simple and efficient iterative algorithm. *J. Chem. Theory Comput.* **2023**, *19*, 9025–9031.
28. Cossi, M.; Barone, V.; Robb, M.A. A direct procedure for the evaluation of solvent effects in MC-SCF calculations. *J. Chem. Phys.* **1999**, *111*, 5295–5302.
29. Hedegård, E.D.; List, N.H.; Jensen, H.J.A.; et al. The multi-configuration self-consistent field method within a polarizable embedded framework. *J. Chem. Phys.* **2013**, *139*, 044101.
30. Li, Q.; Mennucci, B.; Robb, M.A.; et al. Polarizable QM/MM multiconfiguration self-consistent field approach with state-specific corrections: Environment effects on cytosine absorption spectrum. *J. Chem. Theor. Comput.* **2015**, *11*, 1674–1682.
31. Liu, H.; Jenkins, A.J.; Wildman, A.; et al. Time-Dependent Complete Active Space Embedded in a Polarizable Force Field. *J. Chem. Theor. Comput.* **2019**, *15*, 1633–1641.
32. Song, C. State averaged CASSCF in AMOEBA polarizable water model for simulating nonadiabatic molecular dynamics with nonequilibrium solvation effects. *J. Chem. Phys.* **2023**, *158*, 014101.
33. Song, C.; Wang, L.P. A Polarizable QM/MM Model That Combines the State-Averaged CASSCF and AMOEBA Force Field for Photoreactions in Proteins. *J. Chem. Theory Comput.* **2024**, *20*, 6632–6651.
34. Sepali, C.; Goletto, L.; Lafiosca, P.; et al. Fully Polarizable Multiconfigurational Self-Consistent Field/Fluctuating Charges Approach. *J. Chem. Theory Comput.* **2024**, *20*, 9954–9967.
35. Nottoli, T.; Bondanza, M.; Lipparini, F.; et al. A Polarizable CASSCF/MM Approach Using the Interface Between OpenMMPol Library and Cfour. *J. Comput. Chem.* **2025**, *46*, e27550.
36. Mazza, F.; Trinari, M.; Sepali, C.; et al. Analytical Nuclear Gradients for the Multiconfigurational Self-Consistent Field Method Coupled with the Polarizable Fluctuating Charges Model. *arXiv* **2025**, arXiv:2511.10295.
37. Ponder, J.W.; Wu, C.; Ren, P.; et al. Current status of the AMOEBA polarizable force field. *J. Phys. Chem. B* **2010**, *114*, 2549–2564.
38. Bondanza, M.; Nottoli, T.; Nottoli, M.; et al. The OpenMMPol library for polarizable QM/MM calculations of properties and dynamics. *J. Chem. Phys.* **2024**, *160*, 134106.
39. Sorigué, D.; Légeret, B.; Cuiné, S.; et al. An algal photoenzyme converts fatty acids to hydrocarbons. *Science* **2017**, *357*, 903–907.
40. Sorigué, D.; Hadjidemetriou, K.; Blangy, S.; et al. Mechanism and dynamics of fatty acid photodecarboxylase. *Science* **2021**, *372*, eabd5687.
41. Nottoli, M.; Lipparini, F. General formulation of polarizable embedding models and of their coupling. *J. Chem. Phys.* **2020**, *153*, 224108.
42. Jensen, H.J.; Jørgensen, P. A direct approach to second-order MCSCF calculations using a norm extended optimization scheme. *J. Chem. Phys.* **1984**, *80*, 1204–1214.
43. Lipparini, F.; Lagardère, L.; Stamm, B.; et al. Scalable Evaluation of Polarization Energy and Associated Forces in Polarizable Molecular Dynamics: I. Toward Massively Parallel Direct Space Computations. *J. Chem. Theory Comput.* **2014**, *10*, 1638–1651.
44. Greengard, L.; Rokhlin, V. A fast algorithm for particle simulations. *J. Comput. Phys.* **1987**, *73*, 325–348.
45. Caprasecca, S.; Jurinovich, S.; Lagardère, L.; et al. Achieving Linear Scaling in Computational Cost for a Fully Polarizable MM/Continuum Embedding. *J. Chem. Theory Comput.* **2015**, *11*, 694–704.
46. Lipparini, F. General Linear Scaling Implementation of Polarizable Embedding Schemes. *J. Chem. Theory Comput.* **2019**, *15*, 4312–4317.
47. Londi, G.; Salvadori, G.; Mazzeo, P.; et al. Protein-Driven Electron-Transfer Process in a Fatty Acid Photodecarboxylase. *JACS Au* **2025**, *5*, 158–168.
48. Martin, R.L. Natural transition orbitals. *J. Chem. Phys.* **2003**, *118*, 4775–4777.